

Crystal orientation dependent intersubband transition in semipolar AlGaN/GaN single quantum well for optoelectronic applications

Houqiang Fu, Zhijian Lu, Xuanqi Huang, Hong Chen, and Yuji Zhao

Citation: *Journal of Applied Physics* **119**, 174502 (2016); doi: 10.1063/1.4948667

View online: <http://dx.doi.org/10.1063/1.4948667>

View Table of Contents: <http://scitation.aip.org/content/aip/journal/jap/119/17?ver=pdfcov>

Published by the **AIP Publishing**

Articles you may be interested in

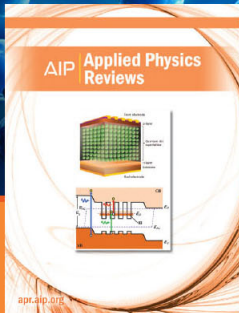
[Temperature dependence of mid-infrared intersubband absorption in AlGaN/GaN multiple quantum wells](#)
Appl. Phys. Lett. **108**, 052102 (2016); 10.1063/1.4941088

[Terahertz absorbing AlGaN/GaN multi-quantum-wells: Demonstration of a robust 4-layer design](#)
Appl. Phys. Lett. **103**, 091108 (2013); 10.1063/1.4819950

[Terahertz intersubband transition in GaN/AlGaN step quantum well](#)
J. Appl. Phys. **113**, 154505 (2013); 10.1063/1.4802496

[Near-infrared two-color intersubband transitions in AlN/GaN coupled double quantum wells](#)
J. Appl. Phys. **105**, 053106 (2009); 10.1063/1.3091280

[Infrared optical absorbance of intersubband transitions in GaN/AlGaN multiple quantum well structures](#)
J. Appl. Phys. **93**, 10140 (2003); 10.1063/1.1577809



NEW Special Topic Sections

NOW ONLINE
Lithium Niobate Properties and Applications:
Reviews of Emerging Trends

AIP | Applied Physics Reviews

Crystal orientation dependent intersubband transition in semipolar AlGaN/GaN single quantum well for optoelectronic applications

Houqiang Fu, Zhijian Lu, Xuanqi Huang, Hong Chen, and Yuji Zhao
 School of Electrical, Computer and Energy Engineering, Arizona State University, Tempe,
 Arizona 85287, USA

(Received 23 February 2016; accepted 23 April 2016; published online 5 May 2016)

The optical properties of intersubband transition in a semipolar AlGaN/GaN single quantum well (SQW) are theoretically studied, and the results are compared with polar c -plane and nonpolar m -plane structures. The intersubband transition frequency, dipole matrix elements, and absorption spectra are calculated for SQW on different semipolar planes. It is found that SQW on a certain group of semipolar planes ($55^\circ < \theta < 90^\circ$ tilted from c -plane) exhibits low transition frequency and long wavelength response with high absorption quantum efficiency, which is attributed to the weak polarization-related effects. Furthermore, these semipolar SQWs show tunable transition frequency and absorption wavelength with different quantum well thicknesses, and stable device performance can be achieved with changing barrier thickness and Al compositions. All the results indicate that the semipolar AlGaN/GaN quantum wells are promising candidate for the design and fabrication of high performance low frequency and long wavelength optoelectronic devices. *Published by AIP Publishing.* [<http://dx.doi.org/10.1063/1.4948667>]

I. INTRODUCTION

Wurtzite (Al, Ga, In)N wide bandgap III-nitride semiconductors have attracted tremendous attention due to their successful applications in blue and green light-emitting diodes (LEDs) and laser diodes (LDs), which enable efficient solid-state lighting and full-color displays.^{1–5} Recently, III-nitride materials have also been studied for intersubband transition (ISBT) based optoelectronics such as quantum well infrared photodetectors (QWIPs),⁶ quantum cascade detectors (QCDs),⁷ and quantum cascade lasers (QCLs).⁸ Because of their advantageous material properties such as large longitudinal photon energy and large band offset,⁸ they offer excellent device performance for high temperature low-frequency (such as 1–10 THz) and long-wavelength (such as infrared 30–300 μm) applications.^{9,10}

Because of different polarization-related effects, III-nitride materials can be divided into three categories: polar c -plane when $\theta = 0^\circ$, semipolar planes when $0^\circ < \theta < 90^\circ$, and nonpolar plane (typically m -plane) when $\theta = 90^\circ$, where θ is the inclination angle of the crystal plane from c -plane.¹¹ Till date, the majority of the studies on III-nitride ISBT has been focused on conventional polar c -plane III-nitride materials.^{6–10} However, these c -plane ISBT devices suffer from the tilted quantum well (QW) profile due to the large polarization-induced electric field inside the QWs. As a result, most ISBT of these c -plane devices is limited to short wavelength regime. For example, Iizuka *et al.* showed GaN/AlN QWs with ISBT in the wavelength range of 1.3–2.2 μm .¹² Gmachl *et al.* reported ISBT of AlGaIn/GaN multiple QWs at wavelengths of 1.75–4.2 μm grown on c -plane sapphire substrate.¹³ Though few reports demonstrated THz transition on the c -plane GaN QW, it involved complicated structure design and was operated at an extremely low temperature of 4 K.¹⁴ In order to get rid of the

polarization-related effects, the ISBT device structures based on novel nonpolar m -plane (with crystal inclination angle $\theta = 90^\circ$ from c -plane) III-nitride materials have been proposed. Feezell *et al.* theoretically studied the ISBT properties of nonpolar III-nitride QWs and found that their absorption wavelengths are longer than those of the c -plane QWs.¹⁵ Pesach *et al.* fabricated low temperature (14 K) nonpolar InGaIn/AlGaIn QW infrared photodetectors with a longest wavelength of 9.3 μm .¹⁶ Edmunds *et al.* reported THz ISBT in the m -plane AlGaIn/GaN QWs.¹⁷ However, the operation temperature (9 K) was too low for practical applications. Other reports can be found in Ref. 18. Despite their appealing properties, the growth challenges such as stacking faults and alloy inhomogeneity^{19–21} have made it very difficult to fabricate high quality nonpolar QWs. Recently, optoelectronic devices grown on semipolar III-nitride substrates ($0^\circ < \theta < 90^\circ$) have gained considerable interests, and high performance LEDs and LDs have been achieved.^{21–25} The advantage of semipolar QWs over nonpolar structures is the much improved material epitaxial quality²¹ while keeping the weak polarization properties.¹¹ Researchers from CNRS group first studied the ISBT on (11 $\bar{2}$) GaN/AlN QWs with wavelength of 1.5–4.5 μm ,^{26,27} which is comparable to some m -plane devices.¹⁸ Despite this encouraging result, the report on semipolar III-nitride ISBT is very limited, and their fundamental physical process is still unclear.

In this work, we systematically study theoretical optical properties of ISBT for AlGaIn/GaN single quantum well (SQW) on semipolar III-nitride planes, while results on polar c -plane and nonpolar m -plane are also obtained. By examining the ISBT frequency, dipole matrix elements, and absorption spectra, we find that nonpolar and certain semipolar planes ($55^\circ < \theta < 90^\circ$) have the optimal performance for ISBT devices with high absorption quantum efficiency (QE). SQW on these semipolar planes show low transition energy

and long wavelength response by increasing QW thickness. The paper is organized as follows: in Section II, we describe the details of the simulation methods; in Section III A, we study ISBT properties of different semipolar AlGaIn/GaN SQW and identify suitable semipolar polar orientations for device applications; in Section III B, two specific semipolar planes ($10\bar{1}3$) ($\theta=32^\circ$, strong polarization) and ($20\bar{2}1$) ($\theta=75^\circ$, weak polarization) are studied with different QW thicknesses, barrier thicknesses, and barrier Al composition, and their device performances are compared.

II. SIMULATION METHODS

ISBT properties of semipolar AlGaIn/GaN SQW are theoretically studied for optoelectronic applications, or specifically for photodetectors. QW structures with different QW thicknesses, barrier thicknesses, and barrier Al composition are calculated and the results are discussed. To calculate the QW bandstructures and subband wavefunctions, we use a commercial software SiLENSe developed by STR Group,²⁸ where one-dimensional Schrödinger-Poisson equation is solved self-consistently with drift-diffusion model included based on the effective mass approximation. The simulation includes the effects of strain and polarization for arbitrary crystal orientations (i.e., polar, nonpolar, and semipolar) of III-nitride materials, which are critical for this work. The elastic constants and piezoelectric coefficients of the software used are listed in Table I. For AlGaIn/GaN heterostructure, the total polarization (P_{tot}) is the sum of piezoelectric polarization P_{pz} and spontaneous polarization P_{sp} . The polarization charge σ at the interface is given by²⁹

$$\begin{aligned}\sigma &= (P_{\text{pz}}^{\text{AlGaIn}} + P_{\text{sp}}^{\text{AlGaIn}}) - (P_{\text{pz}}^{\text{GaN}} + P_{\text{sp}}^{\text{GaN}}) \\ &= -(\Delta P_{\text{pz}} + \Delta P_{\text{sp}}),\end{aligned}\quad (1)$$

where $P_{\text{pz}}^{\text{AlGaIn}}$ and $P_{\text{sp}}^{\text{AlGaIn}}$ are the piezoelectric and spontaneous polarization of AlGaIn barrier, respectively; $P_{\text{pz}}^{\text{GaN}}$ and $P_{\text{sp}}^{\text{GaN}}$ are the piezoelectric and spontaneous polarization of the GaN QW layer, respectively; and ΔP_{pz} and ΔP_{sp} are the difference in piezoelectric and spontaneous polarization between GaN QW layer and AlGaIn barrier layer. For a nonpolar or semipolar plane tilted from c -plane by an angle of θ , the total polarization change that determines the interface charge is expressed as a function of θ by

$$\Delta P_{\text{tot}} = P_{\text{pz}}^{\text{GaN}} + (P_{\text{sp}}^{\text{GaN}} - P_{\text{sp}}^{\text{AlGaIn}}) \cos \theta, \quad (2)$$

where ΔP_{tot} is the total difference of polarization between the GaN layer. $P_{\text{pz}}^{\text{GaN}}$ is the strain-induced piezoelectric

TABLE I. Elastic constants and piezoelectric coefficients used in SiLENSe to calculate spontaneous polarization and piezoelectric polarization.

	Elastic constant (GPa)					Piezoelectric coefficient (C/cm ²)			
	C ₁₁	C ₁₂	C ₁₃	C ₃₃	C ₄₄	e ₁₅	e ₃₁	e ₃₃	P _{sp}
GaN	375	140	105	395	100	-0.27	-0.33	0.65	-0.029
AlN	395	140	115	385	120	-0.48	-0.58	1.55	-0.081

polarization in the GaN layer on top of the AlGaIn barrier layer, which can be expressed as

$$\begin{aligned}P_{\text{pz}}^{\text{GaN}} &= e_{31} \cos \theta \epsilon_{x'x'} + \left(e_{31} \cos^3 \theta + \frac{e_{33} - e_{15}}{2} \sin \theta \sin 2\theta \right) \epsilon_{y'y'} \\ &+ \left(\frac{(e_{31} + e_{15})}{2} \sin \theta \sin 2\theta + e_{33} \cos^3 \theta \right) \epsilon_{z'z'} \\ &+ [(e_{31} - e_{33}) \cos \theta \sin 2\theta + e_{15} \sin \theta \cos 2\theta] \epsilon_{y'z'},\end{aligned}\quad (3)$$

where elements $\epsilon_{k'm'}$ are the strain tensor components and elements e_{ij} are the components of piezoelectric tensor in Voigt notation. From Eqs. (1)–(3), we can see that the polarization and the interface charge are highly dependent on the crystal orientation, which could significantly modify device performances. More detailed calculations of strain and piezoelectric charge in nonpolar and semipolar SQW can be found in Ref. 11. After including the polarization effect, the band diagram, subband wavefunction, and carrier distribution can be calculated using the material parameters listed in Table II. The material properties of alloys are obtained based on the Vegard's law. More information about SiLENSe and publications using this software can be found in Ref. 30.

In a QW system, the electron concentration n_i of the i th subband is calculated by the integral of Fermi-Dirac distribution and density of states as follows:

$$n_i = \int_{E_i}^{\infty} \frac{m^*}{\pi \hbar^2} \frac{1}{1 + e^{\frac{E-E_i}{kT}}} dE = \frac{m^* kT}{\pi \hbar^2} \ln \left(1 + e^{\frac{E_f - E_i}{kT}} \right), \quad (4)$$

where m^* is the effective mass, k is the Boltzmann constant, T is the operation temperature, h is the Planck's constant, E_f is the Fermi energy, and E_i is the energy of i th subband. Incorporating the difference in electron concentration between the first two subbands, the ISBT absorption coefficient $\alpha(\lambda)$ between the first two subbands is derived using the Fermi golden rule and can be expressed as follows:^{31,32}

$$\begin{aligned}\alpha(\lambda) &= \frac{8\pi^3 c^2 \mu}{\lambda n_r L} \sin^2 \gamma |M_{12}|^2 \frac{m^* kT}{\pi \hbar^2} \ln \left\{ \frac{1 + \exp[(E_f - E_1)/kT]}{1 + \exp[(E_f - E_2)/kT]} \right\} \\ &\times \frac{h/(2\pi\tau)}{(E_2 - E_1 - hc/\lambda)^2 + [h/(2\pi\tau)]^2},\end{aligned}\quad (5)$$

TABLE II. Material parameters used in SiLENSe software for calculating conduction band, electron wavefunction, and electron concentration.

Material parameter	Unit	AlN	GaN
Energy gap	eV	6.25	3.51
Varshni parameter a	meV/K	1.799	0.909
Varshni parameter b	K	1462	830
Electron affinity	eV	0	1.96
Dielectric constant	...	8.5	8.9
Donor ionization energy	meV	13	13
Electron g-factor	...	2	2
Electron effective mass along axis a	m ₀	0.26	0.2
Electron effective mass along axis c	m ₀	0.25	0.26
Lattice constant a	nm	0.3112	0.3188
Lattice constant c	nm	0.4982	0.5186

where c is the speed of light in vacuum, μ is the permeability of QW material (GaN in this case), λ is wavelength of incident light, n_r is refractive index, L is the QW thickness, γ is the light propagation angle (usually 45° is used to meet the polarization selection rule and increase the light absorption length³²), M_{12} is the dipole matrix element of first two subbands, and τ is the relaxation time. In the calculation of absorption coefficient, the AlGaIn barrier is unintentionally doped (10^{15} cm^{-3}), and the QW is doped in a way to maximize the background limited infrared performance (BLIP) temperature.¹⁵ In the simulation of the conduction bands in Figs. 1 and 9, the QW is undoped for clear manifestation of the polarization effect on different planes, since high QW doping will cause band bending and make it difficult to compare. We will investigate in detail the doping effect in the future publications. Here, we mainly focus on the polarization effect on the transition energy and absorption coefficient and thus do not include the many-body effects. In the calculation of absorption coefficient, we use single effective mass of $0.2 m_0$, where m_0 is free electron mass. From Table II, the electron effective mass along a and c axes are all $0.2 m_0$ for GaN. Though the effective mass is dependent on the crystal orientation, this dependence is noticeable only on hole not on the electron effective mass.³³ The variation in electron effective mass is relatively small, and the impact on ISBT properties is neglected for simplicity. In this work, the temperature T is set as 300 K. n_r for GaN is 2.30,³⁴ μ is calculated by $n_r^2 \mu_0 / \epsilon_r$, where μ_0 is the vacuum permeability and ϵ_r is the relative dielectric constant for GaN (5.37 is used³⁵). The relaxation time τ is determined by the Lorentzian linewidth of the absorption spectrum and 66 fs is used in this simulation.¹⁵

The dipole matrix element M_{12} is defined as

$$M_{12} = e \int_{-\infty}^{\infty} \psi_2^*(z) z \psi_1(z) dz, \quad (6)$$

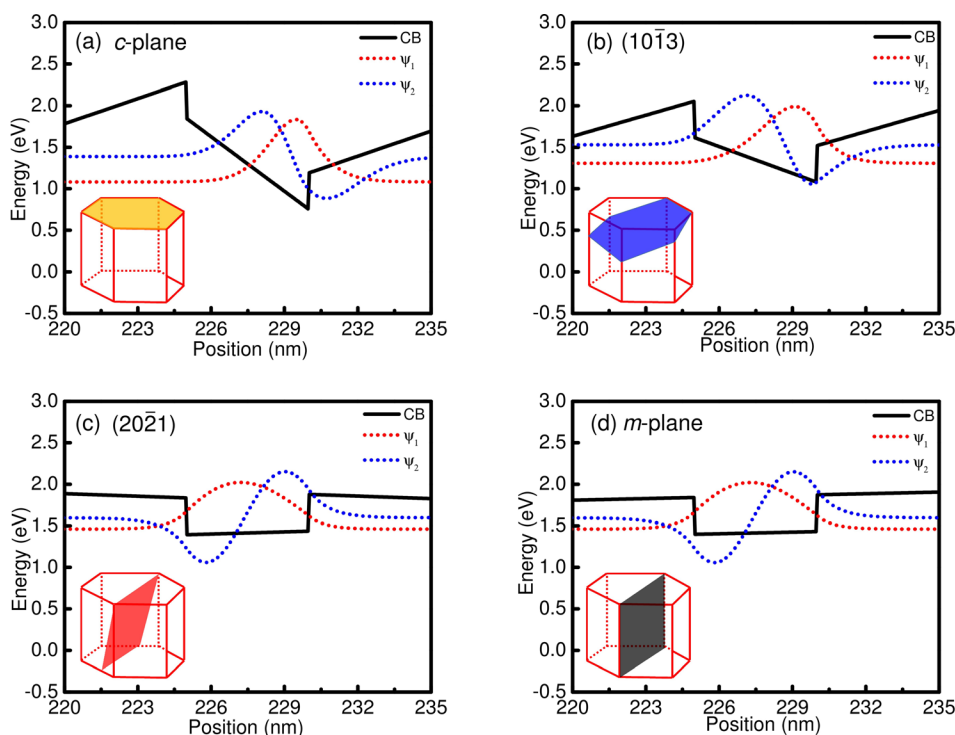


FIG. 1. Conduction band (CB) of $\text{Al}_{0.3}\text{Ga}_{0.7}\text{N}$ (25 nm)/GaN (5 nm) undoped SQW on (a) c -plane, (b) $(10\bar{1}3)$, (c) $(20\bar{2}1)$, and (d) m -plane. The first two subbands' wavefunction ψ_1 and ψ_2 are also shown.

where e is the electron charge, z is the along the device growth direction, ψ_1 is wavefunction of the first subband, and ψ_2 is the wavefunction of the second subband.

III. RESULTS AND DISCUSSION

In Section III A, we first discuss the ISBT properties of AlGaIn/GaN SQW on different crystal orientations. We observed unique properties for certain semipolar planes ($55^\circ < \theta < 90^\circ$): low ISBT frequency, long wavelength response, and high absorption, which are promising for ISBT optoelectronics. In Section III B, we perform detailed studies on QW structures on two particular semipolar planes with different polarization effects, i.e., $(10\bar{1}3)$ ($\theta = 32^\circ$, strong polarization) and $(20\bar{2}1)$ ($\theta = 75^\circ$, weak polarization), where the polar c -plane and the nonpolar m -plane SQWs are also calculated as references. In Section III B 1, we focused on the QW thickness of the structures, which is varied from 3 nm to 12 nm. The semipolar $(20\bar{2}1)$ SQW shows tunable ISBT frequency down to sub-10 THz and absorption wavelength up to $30 \mu\text{m}$. In Sections III B 2 and III B 3, we investigate the ISBT properties of SQW with various barrier thicknesses and Al composition. The polar c -plane and $(10\bar{1}3)$ show higher transition frequency, shorter absorption wavelength, and smaller absorption with increasing barrier thickness and Al composition, which degrades device performance. In contrast, semipolar $(20\bar{2}1)$ SQW shows stable ISBT properties.

A. Crystal orientation

In this section, we investigate the effect of crystal orientation θ on the ISBT properties of $\text{Al}_{0.3}\text{Ga}_{0.7}\text{N}$ (25 nm)/GaN (5 nm) SQW structures on top of 200 nm n-GaN. 30% of aluminum is selected based on the common design of GaAs-based QWIPs. In the polar c -plane SQW, spontaneous

polarization and strain induced piezoelectric polarization result in strong electric field inside the QW. In the nonpolar m -plane case, the polarization is normal to growth direction, which means the polarization-related electric fields do not affect the QW profile. Between these two planes, semipolar planes have reduced polarization effect. In Fig. 1, we calculate the undoped QW conduction band profile of c -plane, m -plane, and two semipolar planes ($10\bar{1}3$) and ($20\bar{2}1$) with the same structure under zero bias. The polar c -plane ($\theta=0^\circ$) and semipolar ($10\bar{1}3$) ($\theta=32^\circ$) SQW show tilted bandstructure while the m -plane ($\theta=90^\circ$) and semipolar ($20\bar{2}1$) ($\theta=75^\circ$) have relatively flat profile. Due to the tilted band profile, the first two subband wavefunction ψ_1 and ψ_2 from c -plane and semipolar ($10\bar{1}3$) structures are largely separated in terms of both energy and position, which will influence dipole matrix elements, ISBT frequency, and absorption coefficients. These results clearly show that polarization-related effects have significant impacts on the ISBT performance of AlGaIn/GaN SQW.

Figure 2 shows ISBT frequencies and matrix elements and for crystal orientation θ from 0° to 90° , where a wide range of semipolar structures are covered. The transition frequency is given by $(E_2 - E_1)/h$. It is noteworthy that the “pair” semipolar planes with different polarities [e.g., ($20\bar{2}1$) at 75° and ($20\bar{2}\bar{1}$) at 105°] have almost identical in their ISBT properties (calculation not shown here). Although the Ga-polar and N-polar QW profiles have opposite QW tilting directions, the impacts on the dipole matrix elements and energy difference of first two subbands are minimum. Therefore, the semipolar structures with θ from 90° to 180° will have similar results to this work. In Fig. 2, the ISBT frequency (in blue) decreases monotonically with θ varying from 0° to 55° . When θ is larger than 55° , minimum difference of ISBT frequency is observed. This trend of transition frequency can be directly linked to the polarization-related effects. With weaker polarizations, QW profile is less tilted and the wavefunctions of subbands are less separated, which will lead to a smaller transition frequency. When a semipolar plane is 45° tilted from c -plane, $\Delta P_{pz}=0$, which is marked

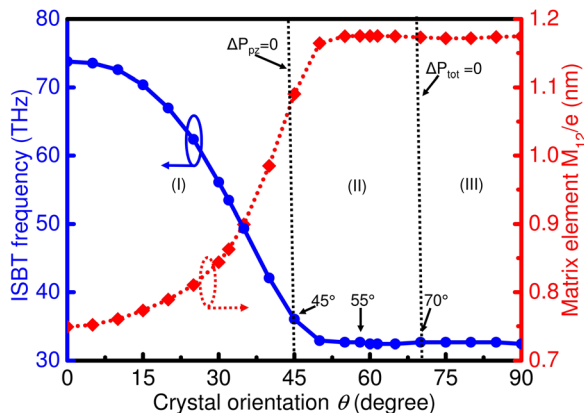


FIG. 2. ISBT frequency and matrix element M_{12}/e and of $\text{Al}_{0.3}\text{Ga}_{0.7}\text{N}$ (25 nm)/GaIn (5 nm) SQW structures on various semipolar plane orientations. The first dashed line is at $\theta=45^\circ$ where piezoelectric polarization $\Delta P_{pz}=0$; the second dashed line is at $\theta=70^\circ$ where the total polarization $\Delta P_{tot}=0$. Three regions (I), (II), and (III) are defined by the two dashed lines.

by the first dashed line in Fig. 2. Although the reduced ΔP_{pz} leads to the decreasing of transition frequency from 0° to 45° , the addition of ΔP_{sp} moves the crossover of ΔP_{tot} to $\theta=70^\circ$, which is marked by the second dashed line in Fig. 2. According to the results in Fig. 2, all the semipolar planes can be divided into three regions: in region I ($0^\circ < \theta < 45^\circ$), the ΔP_{pz} is the dominant effect; in region II ($45^\circ < \theta < 70^\circ$), both ΔP_{pz} and ΔP_{sp} are playing significant roles; in region III ($70^\circ < \theta < 90^\circ$), $\Delta P_{tot} \approx 0$. According to Fig. 2, although the crossover of ΔP_{tot} happens at $\theta=70^\circ$, ΔP_{tot} is already small enough when $\theta > 55^\circ$ and has negligible effects on the QW profile. The simulation shows that the transition frequency of the semipolar ($20\bar{2}1$) structure (region III) can go down to 30 THz, while the frequency of the c -plane structure is still over 80 THz. Therefore, the nonpolar and semipolar planes with $\theta > 55^\circ$ are preferable for lower frequency application. In addition, an opposite trend was also observed for the dipole matrix elements (in red), which can also be explained by the polarization effects. It is shown that semipolar structures with $\theta > 55^\circ$ have very large matrix elements and possibly high absorption coefficients, which is another advantageous feature.

In Fig. 3(a), we calculate the absorption spectra for SQW on the polar c -plane, nonpolar m -plane, and semipolar planes from three regions in Fig. 2. With increasing θ , the spectra of the semipolar planes are moving towards those of the nonpolar m -plane. And the spectrum of ($20\bar{2}1$) and m -plane almost overlap, which makes the semipolar ($20\bar{2}1$) a good alternative of the nonpolar m -plane. Fig. 3(b) shows the peak absorption coefficient and the peak absorption wavelength of SQW with different θ . When $0^\circ < \theta < 55^\circ$, the peak absorption wavelength increases with increasing θ . When $\theta > 55^\circ$, both the parameters reached maxima and the wavelength is kept at $9 \mu\text{m}$ for this particular structure. In terms of peak absorption coefficients, two plateaus are observed. The semipolar planes from regions II ($55^\circ < \theta < 70^\circ$) and III have the highest absorption compared with other semipolar plane orientations. The absorption quantum efficiency (QE) is a critical parameter especially for real device applications, which is given by $\alpha(\lambda)L/\cos\gamma$, where $L/\cos\gamma$ is the light propagation length in devices.³²

The peak absorption QE as a function of peak absorption wavelength (blue squares) for various semipolar structures is illustrated in Fig. 4. Again, all the planes can be categorized into the same three regions: region I represents low absorption and short wavelength region; region II is the transition region; and region III is high absorption and long wavelength region. The results show that the nonpolar and semipolar planes in regions II (when $\theta > 55^\circ$) and III can access to longer wavelength and have higher peak absorption QE, which are desirable for devices operating at long wavelength and low frequency regime. Furthermore, from the perspective of device growth, it is preferable to grow less QWs in order to ensure good material qualities, as the lattice mismatch significantly increases with the number of QWs. In Fig. 4, the 50% absorption QW numbers as a function of peak absorption wavelength (red circles) for different nonpolar and semipolar structures is also illustrated. The 50% absorption QW numbers is the QW numbers when 50% of incident light are

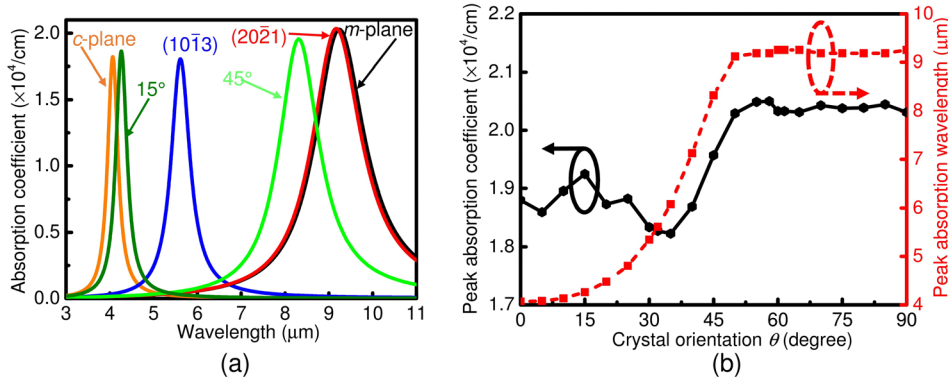


FIG. 3. (a) Absorption spectra for AlGaIn/GaN SQW on different planes including c -plane, m -plane, and four semipolar planes. (b) Peak absorption coefficient and peak absorption wavelength as a function of semipolar plane orientation.

absorbed per round-trip and is given by $N = -\ln(50\%)/(\text{peak absorption QE})$.¹³ It is shown that QW structures on the nonpolar and semipolar planes in regions I and II ($0^\circ < \theta < 55^\circ$) require more QWs to achieve 50% absorption than those on crystal planes in regions II ($55^\circ < \theta < 70^\circ$) and III. In short summary, the results from above two metrics indicate that QWs on the nonpolar and semipolar planes ($55^\circ < \theta < 90^\circ$) will facilitate better performance at longer wavelength regime and has lower material requirement, which are advantageous for device applications.

B. Case studies: c -plane, $(10\bar{1}3)$, $(20\bar{2}1)$, and m -plane

In the following Sections III B 1–III B 3, we focus on two distinct semipolar planes $(10\bar{1}3)$ ($\theta = 32^\circ$, strong polarization) and $(20\bar{2}1)$ ($\theta = 75^\circ$, weak polarization) for more detailed studies, where results on the polar c -plane and nonpolar m -plane are also included as references. The QW thickness, barrier thickness, and barrier Al composition will be modified, and their effects on the ISBT properties will be discussed.

1. Quantum well thickness

The simulated SQW structure has a 25 nm $\text{Al}_{0.3}\text{Ga}_{0.7}\text{N}$ barrier, where the thicknesses of QW is varied from 3 nm (typical thickness of c -plane QW) to 12 nm (thickest QW reported for the semipolar planes³⁶). Figure 5 shows the dipole matrix element and ISBT frequency of the SQW on the semipolar $(20\bar{2}1)$, $(10\bar{1}3)$, c -plane, and m -plane. The semipolar $(20\bar{2}1)$ and nonpolar m -plane SQW have lower

transition frequency at any given QW thickness than that on the semipolar $(10\bar{1}3)$ and c -plane SQW. Furthermore, the transition frequency of semipolar $(20\bar{2}1)$ plane decreases with increasing QW thickness. Due to largely reduced polarization-related effects, the QW profile on the semipolar $(20\bar{2}1)$ plane can be approximately treated as a square finite potential well, for which the quantum mechanical calculation indicates the energy separation of the subbands and transition frequency are inversely proportional to the well thickness.³² In contrast, for the semipolar $(10\bar{1}3)$ structures with strong polarization-related effects, the transition frequency first decreases with increasing QW thickness and then stays almost constant. This is because of the triangular potential well on the semipolar $(10\bar{1}3)$ plane due to the large residual polarizations, which limits the separation of subband wavefunctions. This is more evident in the case of c -plane QW structures with the strongest polarization effects, where changing the QW thickness barely influences the transition frequency. In summary, the semipolar $(20\bar{2}1)$ SQW shows great advantages with tunable ISB transition frequency reaching to a much lower frequency regime. In addition, both semipolar $(20\bar{2}1)$ and m -plane SQW have larger dipole matrix elements which contribute to higher absorption at the same QW thickness.

Figures 6(a)–6(c) show the absorption spectra for c -plane, $(10\bar{1}3)$, and $(20\bar{2}1)$ SQW with different QW

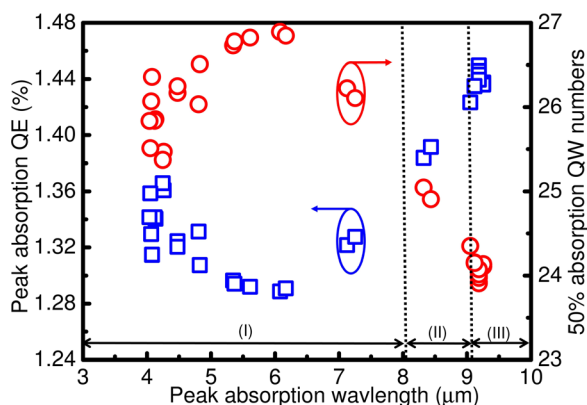


FIG. 4. Peak absorption QE and 50% absorption QW numbers versus peak absorption wavelength, which has been divided into three regions of semipolar plane orientation based QW performance.

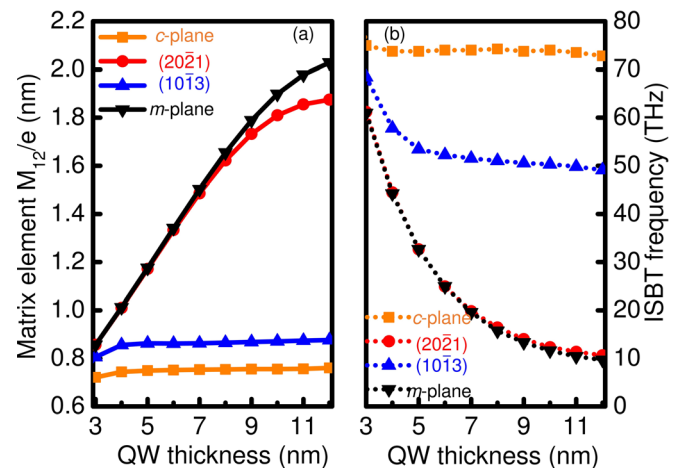


FIG. 5. (a) Matrix element M_{12}/e and (b) ISBT frequency of $\text{Al}_{0.3}\text{Ga}_{0.7}\text{N}$ (25 nm)/GaN SQW as a function of GaN QW thickness on c -plane, $(10\bar{1}3)$, and m -plane.

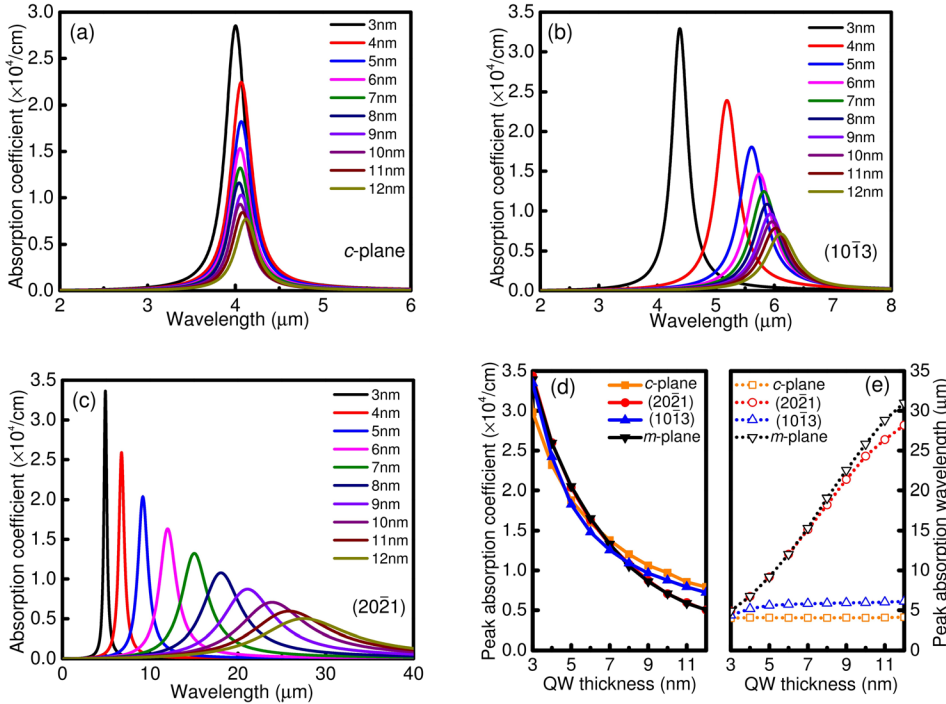


FIG. 6. Absorption spectra of (a) c -plane, (b) $(10\bar{1}3)$, and (c) $(20\bar{2}1)$ 25 nm $\text{Al}_{0.3}\text{Ga}_{0.7}\text{N}/\text{GaN}$ SQW varying QW thickness from 3 nm to 12 nm. Peak absorption coefficient (d) and peak absorption wavelength (e) as a function of QW thickness for c -plane, $(20\bar{2}1)$, $(10\bar{1}3)$, and m -plane $\text{Al}_{0.3}\text{Ga}_{0.7}\text{N}$ (25 nm)/GaN SQW.

thicknesses. Fig. 6(d) summarizes the peak absorption coefficient and peak absorption wavelength for different planes. All the spectra of the c -plane SQW are centralized at a peak wavelength around $4\ \mu\text{m}$. In the case of semipolar $(10\bar{1}3)$ SQW, although the first two spectra are separated, the rest are accumulated at a peak wavelength of $6\ \mu\text{m}$. In contrast, the semipolar $(20\bar{2}1)$ SQW has much dispersive distribution of absorption spectra along the wavelength range. At QW thickness of 12 nm, the peak absorption wavelength is around $28\ \mu\text{m}$ (far infrared). Therefore, the semipolar $(20\bar{2}1)$ SQW can facilitate longer wavelength operation without a much reduction in absorption, which cannot be achieved using the semipolar $(10\bar{1}3)$ plane. Peak absorption occurs when $hc/\lambda = E_2 - E_1$. For all four samples, the peak absorption coefficient decreases with increasing QW thickness. Though thicker QW will reduce the energy separation between the first two subbands, the electron occupation term in Eq. (5), which is proportional to $(n_1 - n_2)$ according to Eq. (4), is less effected since n_1 is still much larger than n_2 and BILP condition is applied ($E_f - E_1 = kT$). The combination of increasing peak absorption wavelength and QW thickness reduces the peak absorption coefficients despite there is an increase in matrix element according to Eq. (5).

2. Barrier thickness

In this section, we study the ISBT properties of $\text{Al}_{0.3}\text{Ga}_{0.7}\text{N}/\text{GaN}$ (5 nm) SQW with barrier thickness varying from 5 nm to 25 nm. Figure 7 presents the dipole matrix elements and ISB transition frequency of semipolar $(20\bar{2}1)$, $(10\bar{1}3)$, polar c -plane and nonpolar m -plane SQW. For the semipolar $(10\bar{1}3)$ and c -plane SQW, the transition frequency dramatically increases with the barrier thickness and the dipole matrix elements are largely reduced. On the other hand, the semipolar $(20\bar{2}1)$ SQW does not show any degradation in the transition frequency and dipole matrix

elements. Therefore, the semipolar $(20\bar{2}1)$ based ISBT devices could offer stable performance even though the barrier thickness are varied during device growth. Figures 8(a)–8(c) show the absorption spectra of SQW with various barrier thicknesses on different planes. Fig. 8(d) shows the peak absorption coefficient and peak absorption wavelength. In the case of the semipolar $(20\bar{2}1)$ SQW, almost all the spectra are overlapped at a peak absorption wavelength of $9\ \mu\text{m}$. For the semipolar $(10\bar{1}3)$ and c -plane SQW, increasing barrier thickness moves their absorption spectra towards much shorter wavelength. Furthermore, the reduction in peak absorption coefficients is also observed for semipolar $(10\bar{1}3)$ and c -plane SQW. Therefore, thick barriers will adversely affect the device performance of the semipolar $(10\bar{1}3)$ and c -plane SQW, while have minimum influence on the semipolar $(20\bar{2}1)$ and m -plane SQW.

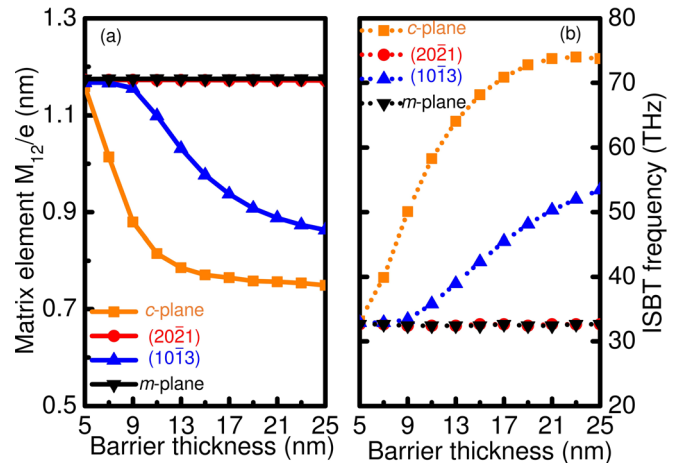


FIG. 7. (a) Matrix element M_{12}/e and (b) ISBT frequency of $\text{Al}_{0.3}\text{Ga}_{0.7}\text{N}/\text{GaN}$ (5 nm) SQW as a function of barrier thickness on c -plane, $(20\bar{2}1)$, $(10\bar{1}3)$, and m -plane.

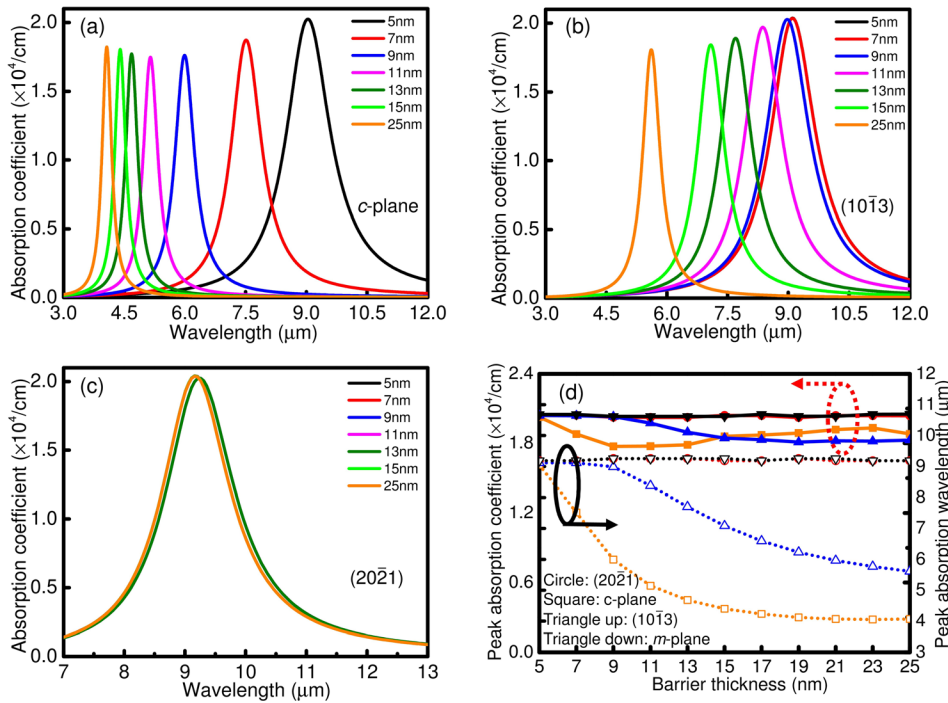


FIG. 8. Absorption spectra of (a) *c*-plane, (b) $(10\bar{1}3)$, and (c) $(20\bar{2}1)$ $\text{Al}_{0.3}\text{Ga}_{0.7}\text{N}/\text{GaN}$ (5 nm) SQW varying barrier thickness from 5 nm to 25 nm. Most of the spectra of $(20\bar{2}1)$ QW with different barrier thicknesses are overlapped. (d) Peak absorption coefficient and peak absorption wavelength as a function of barrier thickness for *c*-plane, $(20\bar{2}1)$, $(10\bar{1}3)$, and *m*-plane $\text{Al}_{0.3}\text{Ga}_{0.7}\text{N}/\text{GaN}$ SQW.

The influence of barrier thickness on the device performance is explained in Fig. 9, where we plot the undoped QW profile with barrier thicknesses of 9 nm, 17 nm, and 25 nm for above four planes. In the case of *c*-plane and $(10\bar{1}3)$ SQW, the profile gets more bent down with increasing barrier thickness. This can further push the subband wavefunctions apart, resulting in an increased ISBT frequency and decreased dipole matrix elements. However, the semipolar $(20\bar{2}1)$ and *m*-plane SQW do not show much change in the QW profile when the barrier thickness is

varied, which could explain the stable performance. With increasing barrier thickness, distances between polarization-induced charges in the QWs are changed. As the result, the electric field in the QW is increased, and the electric field in the barrier is decreased.^{37,38} Therefore, thicker barrier of the *c*-plane and $(10\bar{1}3)$ SQW produces more titling in QW and less tilting in the barrier. It is also shown that the tilting is stronger in the *c*-plane SQW than in the semipolar $(10\bar{1}3)$ SQW because of stronger polarization. Due to negligible or no polarization induced charge at the interface, the QW

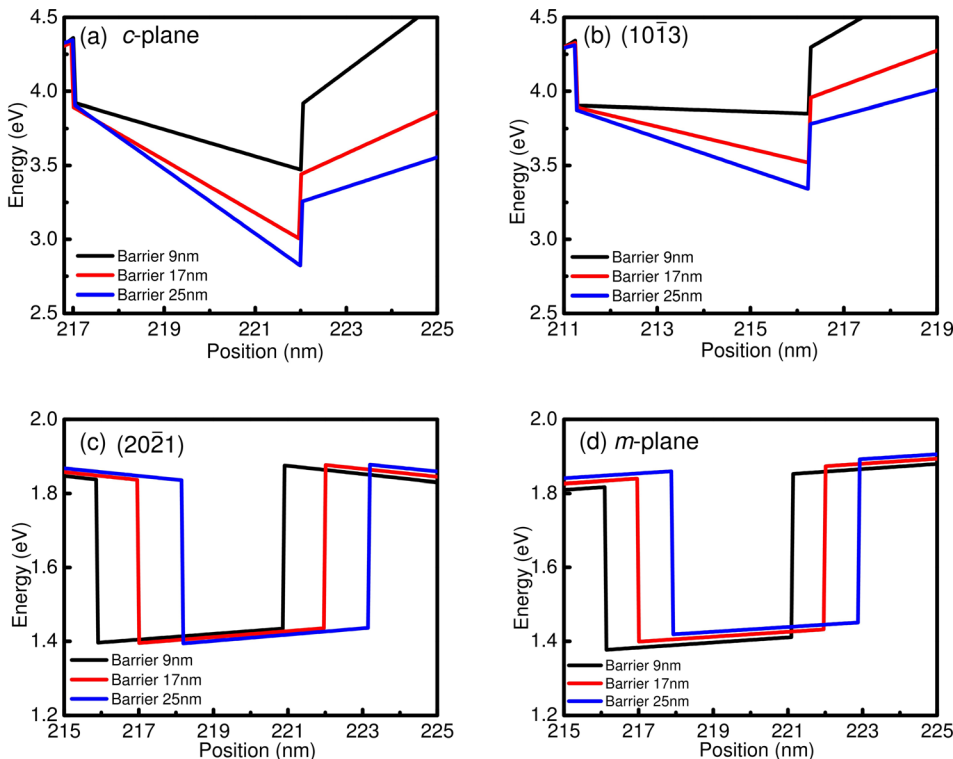


FIG. 9. Conduction band of (a) *c*-plane, (b) $(10\bar{1}3)$, (c) $(20\bar{2}1)$, and (d) *m*-plane $\text{Al}_{0.3}\text{Ga}_{0.7}\text{N}/\text{GaN}$ (5 nm) undoped SQW with barrier thicknesses of 9 nm, 17 nm, and 25 nm.

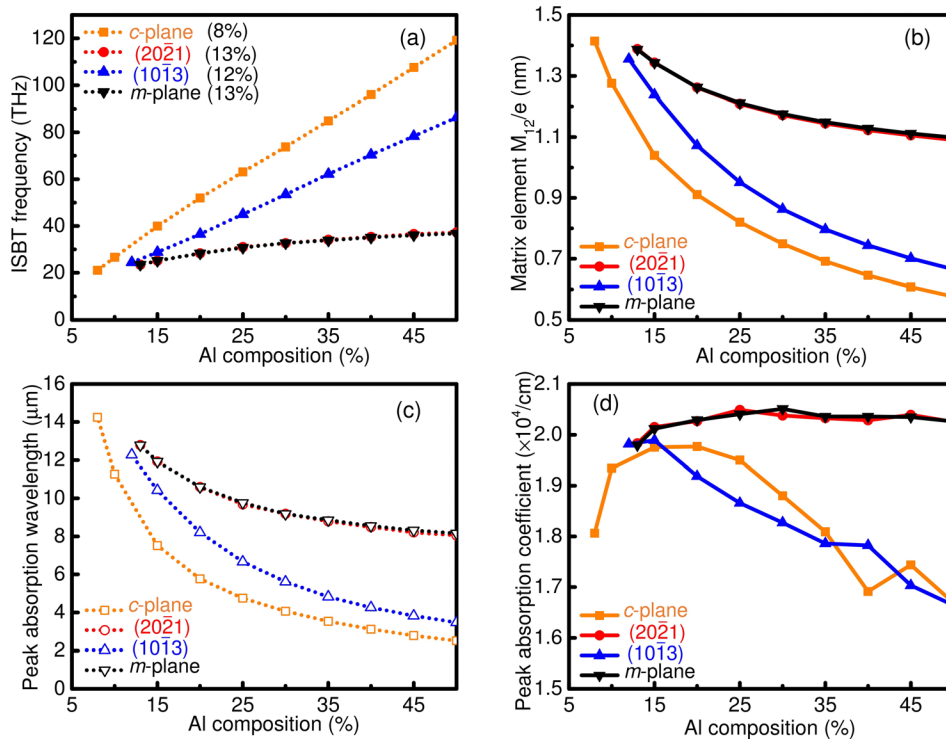


FIG. 10. (a) ISBT frequency and (b) matrix element M_{12}/e of AlGaIn (25 nm)/GaIn (5 nm) SQW as a function of Al composition of barrier on c -plane, (20 $\bar{2}$ 1), (10 $\bar{1}$ 3), and m -plane. In (b), the listed composition (8%, 13%, 12%, and 13%) are the minimum Al composition needed to ensure two subbands in the SQW on different planes. (c) Peak absorption wavelength and (d) peak absorption coefficient as a function of barrier Al composition for different SQW.

profiles of semipolar (20 $\bar{2}$ 1) and m -plane are not influenced by barrier thickness.

3. Barrier Al composition

We also study the effect of barrier Al composition on the ISBT properties of the semipolar SQW. Figures 10(a) and 10(b) show the ISBT frequency and dipole matrix elements, respectively. The Al composition next to the legends are the minimum Al composition required to have two subbands in the QW. With increasing Al composition, the transition frequencies of the semipolar (10 $\bar{1}$ 3) and c -plane SQW experience a dramatic increase, while those of (20 $\bar{2}$ 1) and m -plane SQW are mostly stable. This is because high Al composition will lead to strong ΔP_{pz} and ΔP_{tot} , which make the QW profile more tilted for the semipolar (10 $\bar{1}$ 3) and c -plane SQW. Furthermore, the dipole matrix elements on the semipolar (10 $\bar{1}$ 3) and c -plane SQW are also largely reduced by high Al composition in the barrier. Figures 10(c) and 10(d) describe the peak absorption coefficients and peak absorption wavelength as a function of Al composition. The peak absorption wavelength is decreasing with higher Al composition. But the wavelength reduction is relatively smaller for the semipolar (20 $\bar{2}$ 1) SQW than the (10 $\bar{1}$ 3) and c -plane SQW. And the peak absorption coefficients of (20 $\bar{2}$ 1) SQW remain constant with increasing Al composition. This indicates that at the same Al composition, the semipolar (20 $\bar{2}$ 1) SQW with high absorption coefficients will behave much better in long wavelength optoelectronics.

IV. CONCLUSIONS

We study the ISBT properties of semipolar AlGaIn/GaIn SQW. The semipolar planes in the range of $55^\circ < \theta < 90^\circ$ exhibit a unique shorter ISBT frequency and longer

wavelength response. In addition, they have high absorption coefficients and absorption quantum efficiency, and has lower requirement in QW structures to absorb 50% incident light. The effect of QW thickness, barrier thickness, and barrier Al composition on the ISBT properties of the semipolar (20 $\bar{2}$ 1) (weak polarization) and semipolar (10 $\bar{1}$ 3) (strong polarization) SQW are studied in detail. The semipolar (20 $\bar{2}$ 1) SQW shows tunable transition frequency and absorption wavelength with high absorption coefficients when varying QW thickness. It also shows stable device performance when the barrier thickness and Al composition are changed. All these results indicate that semipolar planes with weak polarization can be used to fabricate high performance low frequency and long wavelength optoelectronic devices.

ACKNOWLEDGMENTS

This work was supported by Bisgrove Scholar program from Science Foundation Arizona.

- ¹S. Nakamura, T. Mukai, and M. Senoh, *Appl. Phys. Lett.* **64**, 1687 (1994).
- ²S. Nakamura, G. Fasol, and S. J. Pearton, *The Blue Laser Diode: The Complete Story*, 2nd ed. (Springer, 2000).
- ³Y. Zhao, J. Sonoda, I. Koslow, C. C. Pan, H. Ohta, J. S. Ha, S. P. Denbaars, and S. Nakamura, *Jpn. J. Appl. Phys., Part 1* **49**, 070206 (2010).
- ⁴Y. Enya, Y. Yoshizumi, T. Kyono, K. Akita, M. Ueno, M. Adachi, T. Sumitomo, S. Tokuyama, T. Ikegami, K. Katayama, and T. Nakamura, *Appl. Phys. Express* **2**, 082101 (2009).
- ⁵Y. Zhao, S. H. Oh, F. Wu, Y. Kawaguchi, S. Tanaka, K. Fujito, J. S. Speck, S. P. DenBaars, and S. Nakamura, *Appl. Phys. Express* **6**, 062102 (2013).
- ⁶D. Hofstetter, S. Schad, H. Wu, W. Schaff, and L. Eastman, *Appl. Phys. Lett.* **83**, 572 (2003).
- ⁷S. Sakr, E. Giraud, A. Dussaigne, M. Tchernycheva, N. Grandjean, and F. Julien, *Appl. Phys. Lett.* **100**, 181103 (2012).
- ⁸E. Bellotti, K. Driscoll, T. Moustakas, and R. Paiella, *Appl. Phys. Lett.* **92**, 101112 (2008).
- ⁹H. C. Liu, C. Y. Song, A. J. SpringThorpe, and J. C. Cao, *Appl. Phys. Lett.* **84**, 4068 (2004).

- ¹⁰N. Horiuchi, *Nat. Photonics* **4**, 140 (2010).
- ¹¹A. Romanov, T. Baker, S. Nakamura, and J. Speck, *J. Appl. Phys.* **100**, 023522 (2006).
- ¹²N. Iizuka, K. Kaneko, and N. Suzuki, *Appl. Phys. Lett.* **81**, 1803 (2002).
- ¹³C. Gmachl, H. M. Ng, and A. Y. Cho, *Appl. Phys. Lett.* **77**, 334 (2000).
- ¹⁴H. Machhadani, Y. Kotsar, S. Sakr, M. Tchernycheva, R. Colombelli, J. Mangeney, E. Bellet-Amalric, E. Sargiannidou, E. Monroy, and F. H. Julien, *Appl. Phys. Lett.* **97**, 191101 (2010).
- ¹⁵D. Feezell, Y. Sharma, and S. Krishna, *J. Appl. Phys.* **113**, 133103 (2013).
- ¹⁶A. Pesach, E. Gross, C. Y. Huang, Y. D. Lin, A. Vardi, S. E. Schacham, and G. Bahir, *Appl. Phys. Lett.* **103**, 022110 (2013).
- ¹⁷C. Edmunds, J. Shao, M. Shirazi-HD, M. J. Manfra, and O. Malis, *Appl. Phys. Lett.* **105**, 021109 (2014).
- ¹⁸T. Kotani, M. Arita, and Y. Arakawa, *Appl. Phys. Lett.* **105**, 261108 (2014).
- ¹⁹M. B. Mclaurin, A. Hirai, E. Young, F. Wu, and J. S. Speck, *Jpn. J. Appl. Phys., Part 1* **47**, 5429–5431 (2008).
- ²⁰F. Wu, Y. D. Lin, A. Chakraborty, H. Ohta, S. P. DenBaars, S. Nakamura, and J. S. Speck, *Appl. Phys. Lett.* **96**, 231912 (2010).
- ²¹Y. Zhao, Q. Yan, C. Huang, S. Huang, P. Hsu, S. Tanaka, C. Pan, Y. Kawaguchi, K. Fujito, C. G. Van de Walle, J. Speck, S. DenBaars, S. Nakamura, and D. Feezell, *Appl. Phys. Lett.* **100**, 201108 (2012).
- ²²Y. Zhao, Q. Yan, D. Feezell, K. Fujito, C. G. Van de Walle, J. S. Speck, S. P. DenBaars, and S. Nakamura, *Opt. Express* **21**, A53 (2013).
- ²³Y. Zhao, S. Tanaka, Q. Yan, C. Y. Huang, R. B. Chung, C. C. Pan, K. Fujito, D. Feezell, C. G. Van de Walle, J. S. Speck, S. P. DenBaars, and S. Nakamura, *Appl. Phys. Lett.* **99**, 051109 (2011).
- ²⁴H. Fu, Z. Lu, X. Zhao, Y. Zhang, S. P. DenBaars, S. Nakamura, and Y. Zhao, *J. Disp. Technol.* **PP**(99), 1 (2016).
- ²⁵Y. Zhao, S. Tanaka, C. C. Pan, K. Fujito, D. Feezell, J. S. Speck, S. P. DenBaars, and S. Nakamura, *Appl. Phys. Express* **4**, 082104 (2011).
- ²⁶L. Lahourcade, P. K. Kandaswamy, J. Renard, P. Ruterana, H. Machhadani, M. Tchernycheva, F. H. Julien, B. Gayral, and E. Monroy, *Appl. Phys. Lett.* **93**, 111906 (2008).
- ²⁷H. Machhadani, M. Beeler, S. Sakr, E. Warde, Y. Kotsar, M. Tchernycheva, M. P. Chauvat, P. Ruterana, G. Nataf, Ph. De Mierry, E. Monroy, and F. H. Julien, *J. Appl. Phys.* **113**, 143109 (2013).
- ²⁸V. F. Mymrin, K. A. Bulashevich, N. I. Podolskaya, I. A. Zhmakin, S. Yu. Karpov, and Yu. N. Makarov, *Phys. Status Solidi C* **2**, 2928 (2005).
- ²⁹S. H. Park and S. L. Chuang, *Appl. Phys. Lett.* **76**, 1981 (2000).
- ³⁰See <http://www.str-soft.com/products/SiLENSe/> for more information about physical models and related publications.
- ³¹D. Ahn and S. Chuang, *IEEE J. Quantum Electron.* **23**, 2196 (1987).
- ³²H. Schneider and H. Liu, *Quantum Well Infrared Photodetectors: Physics and Applications* (Springer, Berlin, 2006).
- ³³S. H. Park, *J. Appl. Phys.* **91**, 9904 (2002).
- ³⁴E. Ejder, *Phys. Status Solidi A* **6**, 445–448 (1971).
- ³⁵T. Kawashima, H. Yoshikawa, and S. Adachi, *J. Appl. Phys.* **82**, 3528 (1997).
- ³⁶C. C. Pan, S. Tanaka, F. Wu, Y. Zhao, J. S. Speck, S. Nakamura, S. P. DenBaars, and D. Feezell, *Appl. Phys. Express* **5**, 062103 (2012).
- ³⁷J. J. Wierer, Jr., D. D. Koleske, and S. R. Lee, *Appl. Phys. Lett.* **100**, 111119 (2012).
- ³⁸G. B. Lin, D. Y. Kim, G. Shan, J. Cho, E. F. Schubert, H. Shim, C. Sone, and J. K. Kim, *IEEE Photonics J.* **5**, 1600207 (2013).